Dynamics of the magnetization reversal in Au/Co/Au micrometer-size dot arrays

J.-P. Jamet, S. Lemerle, P. Meyer, and J. Ferré
Laboratoire de Physique des Solides, URA CNRS 02, Bâtiment 510, Université Paris-Sud, 91405 Orsay Cedex, France

B. Bartenlian, N. Bardou, C. Chappert, and P. Veillet
Institut d'Electronique Fondamentale, URA CNRS 22, Bâtiment 220, Université Paris-Sud, 91405 Orsay Cedex, France

F. Rousseaux, D. Decanini, and H. Launois
Laboratoire de Microstructures et Microélectronique, UPR CNRS 20, 196 Avenue H. Ravera, BP107, 92225 Bagneux Cedex, France

(Received 18 December 1997)

In high-quality Au/Co/Au ultrathin films with high perpendicular magnetic anisotropy, magnetization reversal occurs through easy domain-wall (DW) propagation following rare nucleation events, located at major structural defects. By patterning arrays of dots in such films, we block the DW propagation, and thus sample the intrinsic distribution of nucleation sites, improving precision as the dot diameter decreases. In a Au/Co (1 nm)/Au film we have fabricated large area arrays of round dots, with diameters of 1 and 2 μm, leaving aside an unpatterned area as a witness of the magnetization reversal in a ''continuous film'' having undergone all patterning steps. Polar magneto-optical (MO) Kerr effect was used in both global and imaging experiments to accurately measure the hysteresis loops and aftereffect phenomena. We show that, despite limited damage induced by patterning, the expected behavior is indeed observed. A statistical model was developed, assuming an intrinsic distribution of nucleation sites in the initially continuous film, a uniform nucleation volume V_n, and a linear dependence of the nucleation energy barrier $E_n = 2M_S V_n(H_n - H)$ on both applied field H and nucleation field H_n at a given site (M_S is the saturation magnetization). Comparison between experiments and theory shows an excellent overall agreement, and allows one to obtain an approximate view of the distribution of nucleation fields. We could extract two fundamental lengths, the nucleation length ξ_n (related to V_n), and the mean distance l between nucleation sites. ξ_n was found to be equal to 26 ± 1 nm, in good agreement with previous determinations on similar films. l, equal to about 430 nm, could be viewed as a measure of the typical distance between major structural defects in the ''continuous film.'' Our method is indeed a means to characterize nanometer scale magnetic events (reversal of a nucleation volume), using micrometer scale resolution experiments (MO imaging). This is an example of how microfabrication can help us to understand magnetization reversal in a continuous ultrathin film. [S0163-1829(98)04622-0]

I. INTRODUCTION

It is now possible to control the growing process of ultrathin metallic film structures (a few atomic layer thick) and to obtain a deep knowledge of their crystallographic and magnetic properties. Moving one step forward, a lot of research work is now devoted to the realization of well-defined patterned structures, in which more than one dimension becomes comparable to fundamental lengths of magnetism or electronic transport. These structures have a high fundamental interest, and promising applications are expected in the field of magnetoresistive sensors and recording heads,[1,2] or magnetic and magneto-optic high-density storage media or devices.[3–7] Regular arrays of submicronic magnetic dots are for instance good candidates as media for future ultrahigh-density data recording, in which the bit borders would be perfectly defined by patterning.[5] From a more fundamental point of view, such arrays can be considered as model systems to study magnetic behaviors in reduced dimensions. Indeed, lattice structure, dot geometry, dot size, and distance between dots, can be precisely controlled and compared to magnetic characteristic lengths such as domain size,[8] domain-wall width,[9] and dipolar coupling range.[10,11]

Magnetic wires or dot arrays have been made using different techniques, from simply etching a magnetic film through a mask made by standard lithography techniques,[8,12–14] to deposition on a patterned substrate[15] or electrodeposition through an insulating mask.[3,5] Arrays of nanometer size magnetic particles (down to 1 nm in diameter) have been recently fabricated using a scanning tunneling microscopy setup.[16,17] Other groups use laser light interference patterns to create large area arrays of submicrometer size particles.[6,18]

However, up to now most of the papers about magnetization reversal studies of assemblies of particles have been devoted to thick (>10 nm) magnetic dots.[3–12,14,19] Following our preliminary communication,[20] we report here a comprehensive study of the dynamics of magnetization reversal in dot arrays patterned from the ultrathin film structure: Au/Co(1 nm)/Au(111), deposited on a Si/SiO_2 (100 nm) substrate. This system exhibits a strong perpendicular anisotropy,[21] and magnetization reversal is dominated by a domain-wall (DW) motion process involving only a few nucleation centers.[22,23] By patterning dots of decreasing lateral size, we progressively block the wall motion, and thus create *a model system to study the crossover from ''wall*

motion'' to ''domain nucleation'' types of magnetization reversal process. We used x-ray lithography and ion-beam etching[13] to fabricate large area arrays of micron size dots (1 and 2 μm in diameter). Magneto-optical magnetometry and microscopy were then applied to study the dynamics of magnetization reversal in the arrays, in comparison with that of the original film. Domain visualization confirms a magnetization reversal mechanism driven by a large distribution of nucleation fields inside the set of dots.[20] From magnetic aftereffect experiments, we could obtain the histogram of switching fields in each array, then reconstruct the magnetic hysteresis loops, and finally relate the distribution of switching fields to that of the ''continuous film.'' We were also able to study independently the magnetic switching process of each individual dot, and thus to get information on the dynamics of the intrinsic nucleation events, which happen at a scale of a few tens of nm only.

II. SAMPLES AND EXPERIMENTAL TECHNIQUES

The preparation method and the crystalline structure of the ''as-grown'' Au/Co/Au(111) ultrathin film structures have already been reported.[24] The film was grown in an ultrahigh-vacuum chamber by Joule heating (Au) or electron beam (Co) evaporation. First, a 28-nm-thick Au buffer layer was deposited on a flat thermally oxidized silicon wafer ($t_{SiO_2} \sim 100$ nm). Its annealing at 180 °C during 1 h provides an atomically flat polycristalline Au layer, fully textured with the [111] direction perpendicular to the surface. At room temperature, cobalt grows epitaxially on this Au buffer, in a nearly layer by layer mode, with a mostly hcp(0001) structure. A 7.5 nm thick Au capping layer is finally deposited for protection.

The Co film investigated in the present work is five atomic layers thick. In its *as-grown* state (coming out of the deposition unit), such a 10-Å-thick Co film exhibits a large perpendicular magnetic anisotropy.[21] It shows a very square hysteresis loop, since the nucleation field far exceeds the propagation field: as soon as a nucleation event occurs, the magnetization reverses rapidly by DW motion through the entire sample.[22,23]

Arrays of micrometer-size dots were patterned using synchrotron-radiation x-ray lithography and ion-beam milling. On thin films (total thickness below 50 nm), such techniques allow an excellent resolution, better than 50 nm,[13,25] which in the present work warrants that the edge roughness of the dots remain very low.[13] Details of the fabrication of our dot arrays have already been reported elsewhere.[13,20,26] First, the samples are covered with a positive resist (PMMA/MAA copolymer) of thickness about 600 nm. The resist is then annealed at 100 °C for several hours, and exposed to x rays through a specific mask.[25] After development, an array of resist dots is obtained. The unprotected part of the Au/Co/Au film structure is then etched away using ion-beam milling by Ar ions at 500 eV and 0.5 mA/cm^2. The remaining resist is finally removed in an oxygen plasma. This technique of direct etching through a resist mask leaves a small crown of redeposited material around the dot,[13] which is however of no importance here.

For the present study, four 1×1 mm^2 arrays of round dots were patterned on the sample. In each array, the dots have a uniform size and are regularly spaced on a square lattice. The respective ratios of the dot diameter to the lattice periodicity are 1/1.2, 2/2.2, 1/2, 2/4, where all lengths are in μm. Ion-beam milling is performed through an aperture in a molybdenium foil, which keeps unetched a large area of the sample. This part, referred in the following as *continuous film* (CF), has nevertheless undergone all other nanofabrication steps, and thus gives evidence of the damage possibly induced by the patterning process to the *as-grown* sample.

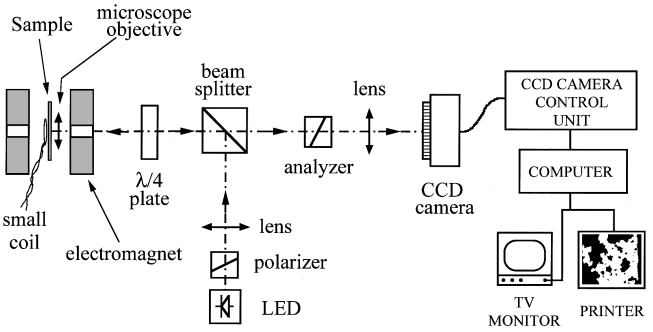

FIG. 1. Polar Kerr experimental setup used for magneto-optical imaging.

We only report here on room-temperature measurements. Polar magneto-optical Kerr effect (PMOKE), measured with a green ($E = 2.29$ eV) He-Ne laser, has been used to determine the magnetic field and time dependence of the magnetization of the CF region or of the patterned dot arrays. In our setup, a slightly focused linearly polarized laser beam is reflected from the sample, and its state of polarization is then analyzed by means of a modulation technique using a photoelastic modulator working at the frequency $f = 50$ kHz.[27,28] The signal is thus averaged over the beam area (about 10^{-2} mm^2). We measure polar Kerr rotation on the zeroth-order light-diffracted beam, i.e., at specular reflection.[29] A nitrogen-cooled coil produces a high enough field (4 kOe) with short (<10 ms) time constant, allowing fast magnetic hysteresis loops and aftereffect measurements.

The polar Kerr microscope (Fig. 1) uses a high intensity (2 mW) blue ($E = 2.76$ eV) light emitting diode (LED) from Nichia Chemical. A cooled charge-coupled device (CCD) camera (512×490 pixels) acquires the images which are stored and later processed in a special unit.[20,22] On the arrays, diffraction effects limit the spatial resolution to about 0.5 μm, i.e., more than the intrinsic resolution of the camera (1 pixel$=0.2 \times 0.2$ μm^2). We obtain the evolution of the magnetic structure by subtracting the image of the saturated sample from that acquired during each step of the magnetization reversal. Analysis of the images can thus yield hysteresis loops for a given assembly of dots as well as for single dots. An electromagnet ($H < 4.5$ kOe) is used for slow or quasistatic magnetic measurements, while a small pulsed copper coil allows us to investigate rapid variations of the magnetization. This coil (20 turns, 1.5 mm inner diameter) is located against the sample on the substrate side, i.e., at a distance of 0.3 mm from the magnetic film. The maximum magnetic field generated by this coil is 7.5 kOe for a 50 A current. We have calibrated it with an accuracy of about 10% by an inductive method using a small three-turns coil with 0.5 mm inner diameter. The current pulses reach 95% of

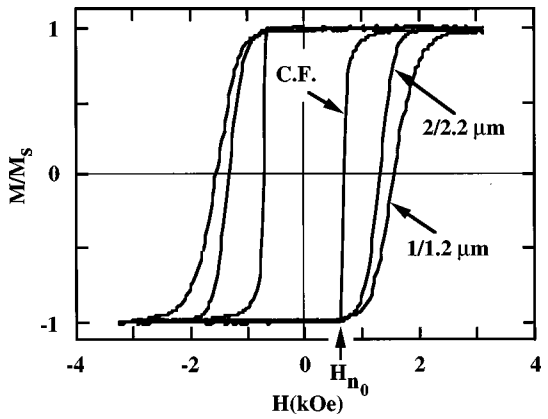

FIG. 2. PMOKE hysteresis loops on the continuous film and on the 1/1.2 and 2/2.2 μm dot arrays. H_{n_0} is the smallest nucleation field value of the continuous film.

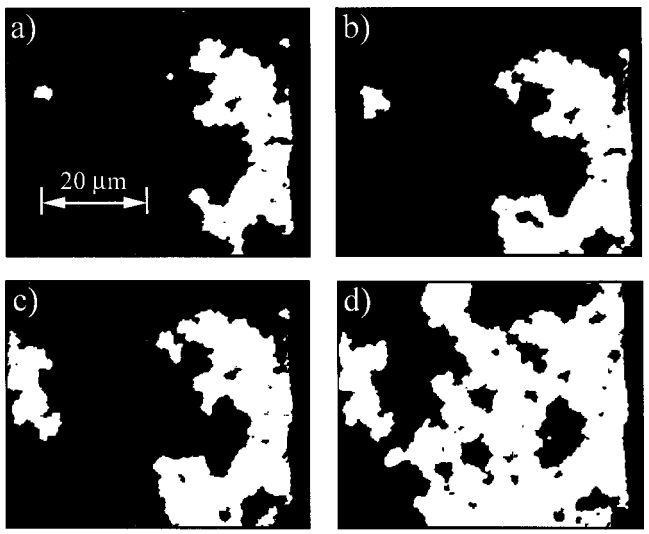

FIG. 3. Magneto-optical images showing the magnetization reversal by DW motion in the continuous film. Each image is obtained after applying n successive field pulses with identical amplitude (0.8 kOe) and width $\Delta t = 45$ μs. The total application time $n\Delta t$ was equal to (a) 0.045 ms, (b) 0.135 ms, (c) 0.45 ms, and (d) 5 ms. The nucleation started essentially on the border of the ''continuous film'' at the right side of the images [Fig. 3(a)]. The white areas indicate magnetization reversal.

their saturation value within about 5 μs. For the present study we only used pulses with a duration $\Delta t = 24$ μs, except for the series of images displayed in Fig. 3 where we used for convenience 45 μs pulses. For longer times, we made a series of 24 μs pulses, with a low repetition rate to avoid the heating of the sample by more than 1 K. For small magnetic fields, it has been previously shown[30] that in such samples the change of the domain pattern produced by a set of n individual pulses with duration Δt is similar to that obtained with a single pulse of the same amplitude and a width equal to $(n\Delta t)$. In our case, this property has been verified on a very extended time range from 10 μs to several thousands of seconds.

III. MAGNETIZATION REVERSAL IN THE CONTINUOUS FILM

The Kerr rotation loop of the CF area (Fig. 2), measured with a focused laser beam, is not as square as the one obtained for the as-grown film and exhibits higher coercivity and larger propagation field distribution.[20] As can be seen from Figs. 2 and 3, the magnetization reversal happens in two stages.

First, a few nucleation events occur at rare sites, followed by a fast magnetization reversal by DW propagation wherever there are only weak pinning energy barriers to overcome (Fig. 3), as already observed for similar unetched type of samples.[22,23] In the following, this process will be referred to as *a weak-pinning-type reversal*.

Then the DW's reach areas surrounded by strong pinning centers, which do not exist in as grown films and can thus be attributed to limited damages induced during the lithography process. The DW winds round these areas, often displaying an irregular shape which is directly connected to the path between strong pinning centers (Fig. 3). Before saturation, domains show a lacunar structure: this phenomenon has been already observed in other ultrathin cobalt films, but at slightly smaller thicknesses.[31,32] To go over these strong pinning energy barriers requires more Zeeman energy, or equivalently longer lag times in relaxation experiments. Thus, as compared to an area with only weak pinning centers and for a given applied field H, the switching of the areas surrounded by strong pinning centers is considerably slowed down, as shown globally through the relaxation of the magnetic aftereffect (Fig. 4). This last behavior will be referred to as *a strong-pinning-type reversal*. The existence of those strong pinning centers explains why, at long times, the final part of the magnetization reversal shown in Fig. 4 still exists over a quite large range of magnetic fields (0.75–1.7 kOe). This also explains the slow saturation in the hysteresis loop (Fig. 2), which demonstrates the presence of a large distribution of local coercivities in large field. *Note however that this strong-pinning regime affects less than 10% of the sample area.*

The magnetic aftereffect phenomenon is only presented at long times in Fig. 4 but relaxation curves have been measured with a high accuracy over the 0.1–50 s time range, for applied fields up to 1.78 kOe, large enough to reach the full magnetic saturation. This allowed us to determine the *demagnetization time* $t_{1/2}$ necessary to reverse half of the magnetization over the typical sample area of 10^{-2} mm^2 sensed

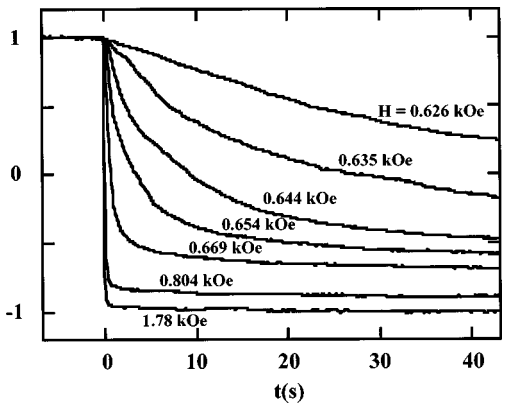

FIG. 4. Magnetic aftereffect in the continuous film measured continuously by PMOKE for several field values.

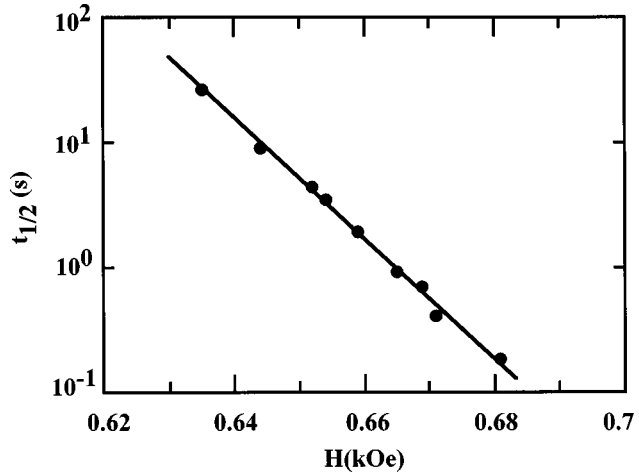

FIG. 5. Magnetic-field dependence of the demagnetization time $t_{1/2}(H)$ of the continuous film extracted from the data depicted in Fig. 4.

by the focused laser beam. Typical values are $t_{1/2}=0.18$ and 27 s, respectively for $H=0.680$ and 0.635 kOe. Such low-field values produce DW motion in the weak-pinning regime, and in agreement with predictions for a thermally activated mechanism,[33] $t_{1/2}$ varies exponentially with H (Fig. 5), according to

$$t_{1/2}=5.2\times 10^{31}\exp(-110H). \tag{1}$$

In this expression $t_{1/2}$ is evaluated in s and H in kOe.

Furthermore, using expression (1) the mean domain-wall velocity at half reversal ($M=0$) can be estimated. It reaches for instance about 0.5 mm/s for 0.68 kOe, and increases very rapidly with field. In weak pinning areas, expression (1) is presumably still valid in fields large enough to reach the viscous regime,[23] i.e., for a typical velocity of 5 m/s which can be obtained under the so-called propagation field $H_p=0.84$ kOe. Let us recall that, in the viscous regime, the domain-wall motion is not thermally activated, contrary to the pinning mechanism.[30]

Hence, from expression (1) we may consider that at fields above 0.78 kOe, corresponding to $t_{1/2}=2.8\ \mu$s for measurements over a 10^{-2} mm^2 area, magnetization reversal in weak-pinning regions happens immediately after nucleation, i.e., in much less than 1 μs at the scale (1 and 2 μm) of the patterned dots in the arrays. This fast reversal, at a micrometer scale, is well revealed in Fig. 3(a).

IV. MAGNETIZATION REVERSAL IN DOT ARRAYS

As was clearly shown in our study of the CF, the microfabrication process induces damage to the as-grown film. We have so far no indication of the exact nature of the defects induced by microfabrication. From test experiments we could however observe that the most damaging step is the first one, i.e., the baking process of the resist after its deposition on the sample. Neither the ion bombardment through the resist layer, nor the final step of removing the resist in an oxygen plasma, significantly influence the magnetic behavior of an as-grown film. *The dot array can thus be envisioned as a geometrical pattern superimposed*, not on the as-grown film, but *on an ''initial continuous film''* that would have had on average the same magnetic properties as the CF area studied above.

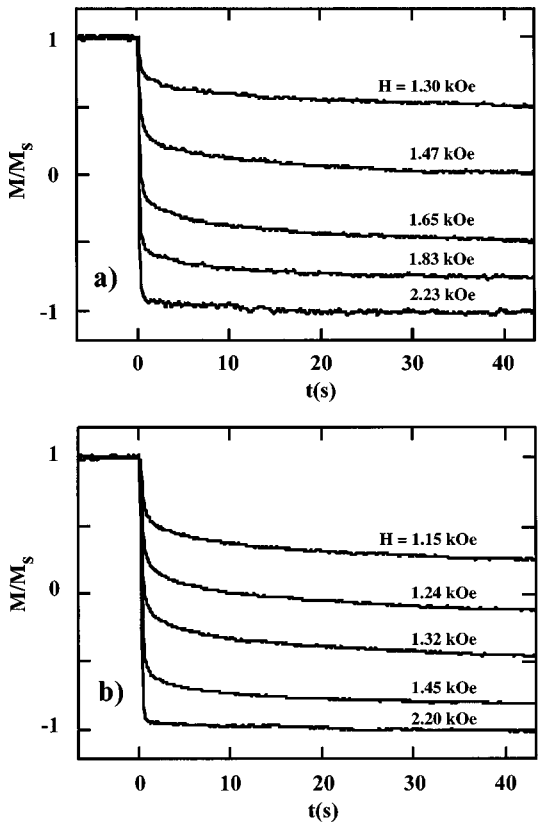

FIG. 6. Magnetic aftereffect in the (a) 1/1.2 μm and (b) 2/2.2 μm arrays measured by PMOKE. The response is averaged over several thousand of dots.

This, of course, totally neglects damage possibly induced at the dots edges during the ion-milling step. We will come back to this point later. Note however that, due to fast redeposition of the Au substrate, the edges of the Co films are certainly buried and thus protected, which is consistent with the fact that no change of the magnetic properties of the arrays could be detected over at least one year.

A. Generalities

The Kerr hysteresis loops of dot arrays are much more rounded than that exhibited by the CF (Fig. 2), and the coercive field drastically increases when reducing the dot size. However, the magnetization reversal starts at the same field value H_{n0} for both the CF and all the investigated dot arrays, which shows that no extra low nucleation field sites exist in the arrays with respect to the CF, in agreement with the discussion above.

We have also verified that the 1/1.2 and 1/2 dot arrays (respectively, the 2/2.2 and 2/4 dot arrays) have identical hysteresis loops. This is consistent with magnetization reversal of noninteracting particles, as will be justified below.

The dynamics of the magnetization reversal for the 1/1.2 and 2/2.2 dot arrays (Fig. 6) differ also drastically from that exhibited by the CF part of the sample (Fig. 4). At a given applied field, after a rapid initial variation the integrated magnetization evolves slowly with time. This is a typical behavior found for systems with a large distribution of en-

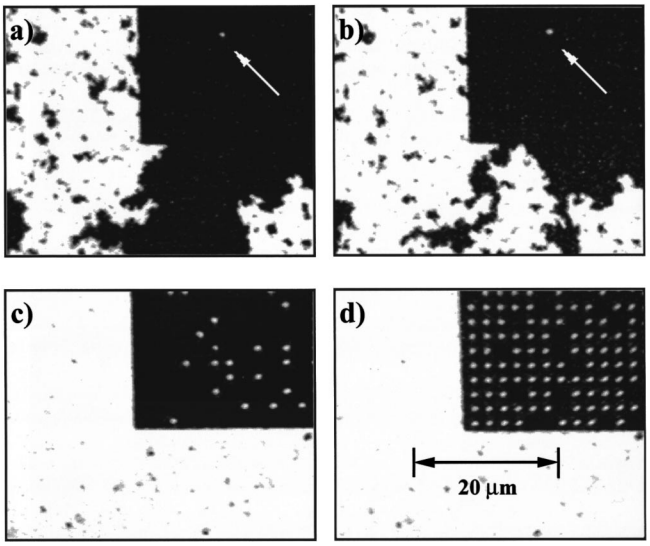

FIG. 7. Magneto-optical images showing the magnetization reversal both in the continuous film and the 1/2 μm dot array parts of the sample: (a) after 10 s under 0.7 kOe, (b) after 100 s under 0.7 kOe, (c) after 10 s under 1.2 kOe, and (d) after 10 s under 1.63 kOe. In (a) and (b) the progressive magnetization reversal at low field of the first switched dot (white arrow) is clearly shown.

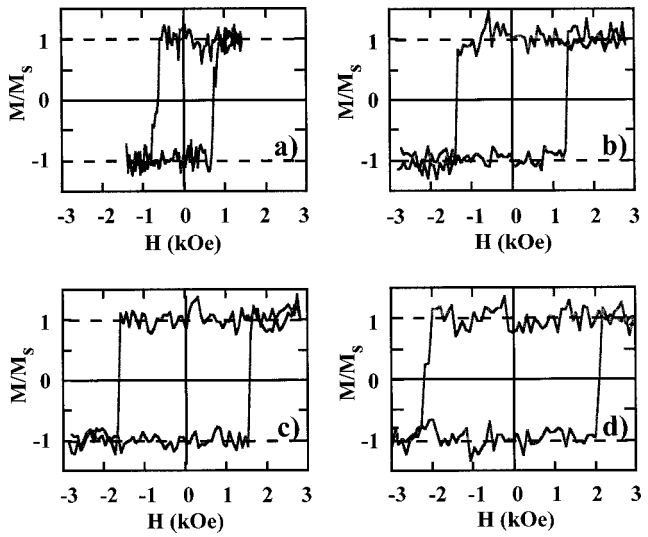

FIG. 8. Individual hysteresis loops of four different dots of Fig. 7, obtained from magneto-optical imaging. Each dot has its own hysteresis loop and coercive field: (a) for the first switched dot [Figs. 7(a), 7(b)] and (b)–(d) for other more typical dots [Figs. 7(c), 7(d)].

ergy barriers, in our case at least one barrier per dot. The type of relaxation shown in Fig. 6 is, for instance, close to that found in films for which magnetization reversal is dominated by progressive nucleation.[22,23] As in the case of the CF area, magnetic aftereffect measurements show that $t_{1/2}$ of a dot array depends exponentially on the applied field, at least over the 0.1–50 s time range, according to

$$t_{1/2}=1.27\times10^{27}\exp(-40H) \quad \text{for the 1/1.2 dot array} \tag{2}$$

$$t_{1/2}=2.44\times10^{27}\exp(-49H) \quad \text{for the 2/2.2 dot array.}$$

As for hysteresis loops, within our experimental precision the dynamics are found to be similar for dot separations of 0.2 or 1 μm, and expressions (2) apply also to the 1/2 and 2/4 dot arrays.

To get more direct information we performed PMOKE domain imaging in a part of the sample covering simultaneously regions of the CF area and one of the dot arrays.

As an example, Figs. 7(a) and 7(b) show the domain configuration for CF and 1/2 dot array, after applying field pulses of $H=0.7$ kOe at 10 and 100 s, respectively. A large portion of the CF area with weak pinning centers is magnetically reversed through DW motion, while only one dot [indicated by an arrow in Figs. 7(a) and 7(b)] is switched over the investigated area. Even though, as can be seen in Fig. 8(a), this particular dot exhibits a nontypical hysteresis loop. It shows a complex reversal behavior in two close successive steps as H is increased, which also explains the change of brightness of its PMOKE image between 10 and 100 s [Figs. 7(a) and 7(b)] and can be attributed to domain-wall depinning inside the dot. As will be discussed below, such a behavior is quite unusual since, in the field and time ranges we explored, the great majority of dots always appear to be fully switched or unswitched with no intermediate situation.

In Figs. 7(a), 7(c), and 7(d) we compare the dynamics of the magnetization reversal under different fields at a fixed time duration of 10 s. In high fields ($H\geqslant1.17$ kOe), the magnetization is completely reversed at saturation in the CF part while magnetic dots are still switching progressively when increasing H, in good agreement with hysteresis loops (Fig. 2) and magnetic aftereffect data (Figs. 4, 6). For a pulse duration of 10 s a complete reversal of all dots in the 1/2 array is obtained only for $H>2.2$ kOe.

Starting from the knowledge of the magnetization reversal mechanisms in the CF studied in Sec. III, and independently of the nucleation process, we have to consider the two limiting situations (weak or strong pinning) inside a given magnetic dot.

Since the domain-wall motion in weak-pinning regions is characterized by a typical activation length of 25 nm,[23] it should not be affected by the micrometer-scale patterning. After nucleation, the characteristic switching time of dots covering only weak-pinning regions may thus be evaluated from expression (1). This means that, even in an applied field equal to the smallest nucleation field H_{n_0} of the CF (cf. Fig. 2), which is of the order of 0.66 kOe, the time for the complete magnetization reversal of a dot is shorter than 0.1 s, i.e., far less than the characteristic time of the imaging experiment reported in Fig. 7. Hence such dots will appear to switch instantaneously after nucleation, as revealed by most of the individual square hysteresis loops of Figs. 8(b)–8(d).

On the other hand, for an area of a dot array patterned over a strong pinning region of the ''initial continuous film,'' the complete reversal can, in principle, only be reached for $H=2.2$ kOe (or much longer waiting times). This should however concern only a small proportion of the dots: according to Fig. 4, 93% of the dots will be already switched under $H=0.8$ kOe, if their corresponding nucleation field is smaller than this field.

To confirm more directly the above arguments, we have estimated the number of dots which are not completely

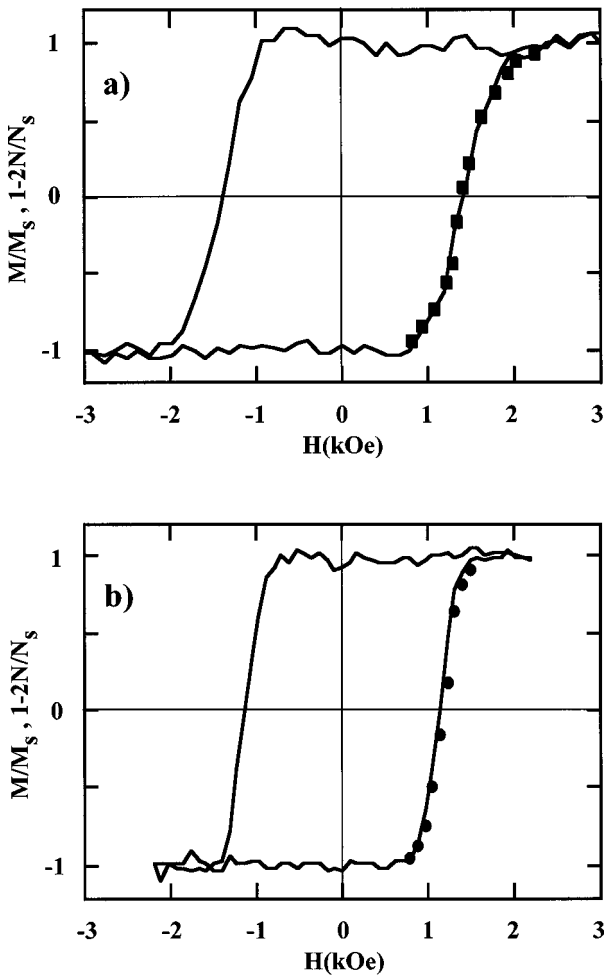

FIG. 9. Hysteresis loops of the (a) 1/1.2 μm and (b) 2/2.2 μm dot arrays measured by two independent imaging methods: by averaging the magneto-optical effect over a limited area of N_S dots (—) or by counting directly the number N of switched dots (symbols) over the same area. The symbols superimpose nicely on the continuous lines.

switched at each field value because of localized hard magnetic centers. To do so, we have compared the polar Kerr amplitude measured for a large assembly of dots (direct integration of the camera signal over the full image window) with the number N of switched dots detected on the image (i.e., at each field value, we have counted the number of reversed dots). Both measurements were done in the same imaging experimental conditions, i.e., N was determined directly from the magnetic image obtained at each field value after its application during 10 s and the Kerr loop was constructed from magneto-optical signals measured at different fields using the same procedure. We effectively checked that, within the experimental errors, we can rebuild the hysteresis loop from the determination of N at each field (Fig. 9). This allows us to conclude that, after nucleation, the magnetization reverses rapidly in at least 95% of the dots, even for those which overlap a strong-pinning region. This was checked further by measuring individual hysteresis loops of dots randomly chosen in the array (Fig. 8).

We finally checked experimentally the negligible role of long-range interactions between dots by proving that the topological distributions of neighboring switched cells is very well described by the expected probability law for independent dots.[34] The effect of the dipolar field on a dot, created by the surrounding dots, has also been calculated. For the closest separation of 0.2 μm between these ultrathin magnetic dots, we estimate a maximum dipolar field of only 11 Oe at their edge, which is far too small as compared with intrinsic nucleation and propagation fields to affect the DW motion and nucleation processes.

The main difference in the magnetization reversal between the CF and dot arrays comes thus from the blocking of the DW propagation at the edge of the dots. The hysteresis loops (Fig. 2) and magnetic aftereffect relaxation curves (Fig. 6), as well as the above discussion, show that the nucleation process plays the major role on the magnetization reversal phenomena of the dot arrays. This explains why the shape of the relaxation curves compares well with the dynamics of a set of independent small particles having distributed time constants.[22,35]

In conclusion, the magnetization reversal of such an assembly of decoupled dots is driven by the distribution of nucleation fields. We shall see now how this distribution can be deduced from the magnetic hysteresis and relaxation data.

B. Distribution of nucleation fields

In too large magnetic particles ($\sim$100 nm),[36,37] the switching probability cannot be strictly described by the Néel-Brown model,[35,38] which assumes thermal activation over a single-energy barrier. Very recently, it was shown by Wernsdorfer *et al.* that this model only applies to sufficiently small Co particles ($\sim$15–30 nm).[39] However, in our dots, since the dynamics is controlled by nucleation, the expected lateral size of a nucleation center is of the order of 25 nm.[30] We shall thus use a Néel-Brown type model to interpret our experimental results, *i.e., we assume that the reversal of a dot occurs initially through a jump over a single barrier.*

The dynamics of magnetization reversal of an assembly of small anisotropic magnetic particles has been investigated by Néel.[35] In the present case of a DW-motion-dominated-type reversal in each dot, switching field or relaxation measurements are testing the dynamics of nucleation. Without any applied field, each dot is characterized by an energy barrier ΔE that we will write in terms of an intrinsic nucleation field H_n so that $\Delta E = 2M_S V_n H_n$.[33] Here, M_S is the saturation magnetization and V_n is the volume of the nucleation center. For the assembly of dots under consideration, we define the distribution $f(H_n)$ of nucleation fields as follows: $f(H_n)dH_n$ is the probability that a given dot has an intrinsic nucleation field in the interval $[H_n, H_n + dH_n]$. This distribution $f(H_n)$ must satisfy the normalization relation $\int_0^\infty f(H_n)dH_n = 1$. From this distribution, we can deduce the number $N(t,H)$ of switched dots at time t and under an applied field H. For a large number N_S of dots

$$N(t,H)/N_S = \int_0^H f(H_n)dH_n + \int_H^\infty \left[1 - \exp\left(-\frac{t}{\tau(H_n,H)}\right)\right] f(H_n)dH_n \quad (3)$$

with a mean switching time $\tau(H_n,H)$:

$$\tau(H_n,H)=\tau_0\exp[2M_SV_n(H_n-H)/kT], \quad (4)$$

$1/\tau_0$ being the attempt frequency [we shall take here $\tau_0=2.5$ ns (Ref. 23)]. The first integral corresponds to the dots which are quasi-instantaneously switched (i.e., the Zeeman energy alone is enough to overcome the switching energy barrier), whereas the second integral refers to the thermally activated magnetization reversal in the dots having an energy barrier stronger than the Zeeman energy. Expression (3) can also be written

$$N(t,H)/N_S=1-\int_H^{\infty}\exp\left(-\frac{t}{\tau(H_n,H)}\right)f(H_n)dH_n. \quad (5)$$

To write expression (4), we assumed that the energy barrier corresponding to an intrinsic nucleation field H_n is proportional to H_n-H. More generally, one expects an energy barrier proportional to $(H_n-H)^{\delta}$, where δ is an exponent characterizing the nucleation process. To take $\delta=1$ has the great advantage that it allows complete analytical calculations which can be further compared to experimental results. Besides, as we shall see below, the good agreement between theory (in the case $\delta=1$) and experiments is another justification of our treatment.

It should also be emphasized that, to deal with our experimental results, it is more appropriate to consider a distribution of nucleation fields as we do, instead of a distribution of energy barriers which include the magnetic field.[30,40] Indeed, at a given temperature, the intrinsic distribution $f(H_n)$ is fixed whatever the applied field value can be. This would not be the case if we considered a distribution of energy barriers since the distribution would be shifted towards zero when increasing the magnetic field.

Following Ref. 40, one can consider that the exponential term inside the integral of expression (5) is equal to 1 for $t<\tau(H_n,H)$ and 0 for $t>\tau(H_n,H)$. This assumption remains valid as long as the distribution width, ΔH_n, of $f(H_n)$ is not too narrow [typically when $\Delta H_n>(kT/2M_SV_n)\ln(t/\tau_0)$]. Then one can write, approximately

$$N(t,H)/N_S\approx\int_0^{H+(kT/2M_SV_n)\ln(t/\tau_0)}f(H_n)dH_n. \quad (6)$$

Besides we can define a mean nucleation field $\overline{H}_n$ such as

$$0.5=\int_0^{\overline{H}_n}f(H_n)dH_n. \quad (7)$$

After introducing the time $t_{1/2}(H)$ necessary to demagnetize the sample (i.e., for $N(t_{1/2}(H),H)/N_S=0.5$), and starting from expressions (6) and (7), we can write

$$H=\overline{H}_n-(kT/2M_SV_n)\ln[t_{1/2}(H)/\tau_0], \quad (8)$$

an expression which can be rewritten

$$t_{1/2}(H)=\tau_0\exp\left(\frac{2M_SV_n}{kT}\overline{H}_n\right)\exp\left(-\frac{2M_SV_n}{kT}H\right). \quad (9)$$

so that expension (6) becomes

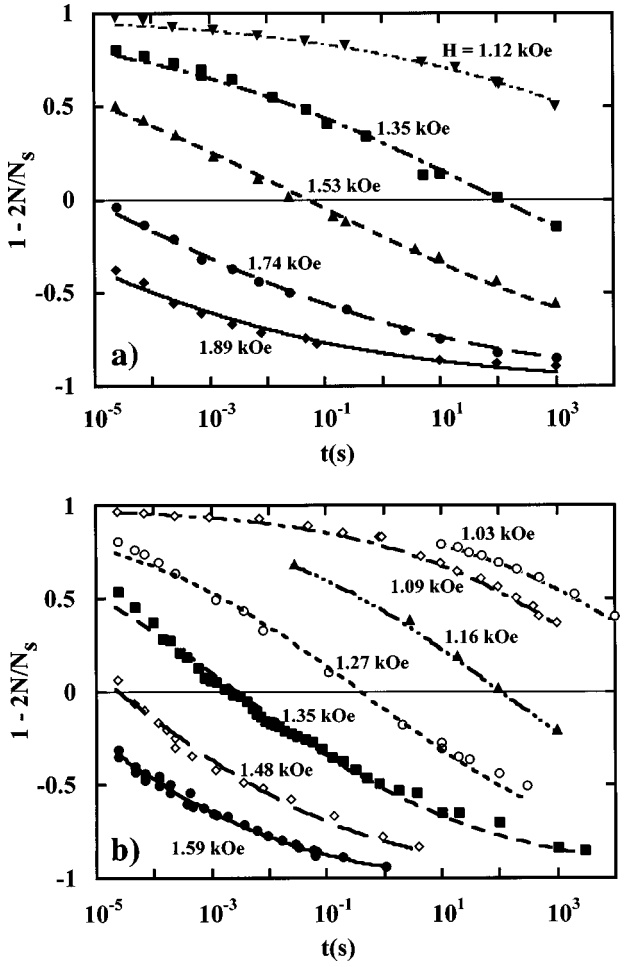

FIG. 10. Magnetic aftereffect in the (a) 1/1.2 μm and (b) 2/2.2 μm dot arrays measured by magneto-optical imaging for various field values. The data have been obtained by counting the number of dots with reversed magnetization for increasing waiting time values. The lines are guides for the eyes. The demagnetizing time $t_{1/2}(H)$ corresponds to $1-2N(H)/N_S=0$.

$$N(t,H)/N_S=\int_0^{\overline{H}_n+(kT/2H_SV_n)\ln[t/t_{1/2}(H)]}f(H_n)d(H_n). \quad (10)$$

It is important to notice that the set of equations (6)–(10) allows a complete description of the magnetization reversal dynamics of a dot array. We shall now use these expressions to extract the nucleation field distribution $f(H_n)$ from experimental results at different applied fields. The measurements have been performed on an assembly of 20×20 dots in the 1/1.2 and 2/2.2 arrays, by counting the number of switched dots (Fig. 10). The sample was first magnetically saturated in a 5 kOe field generated by an electromagnet, applied during several seconds to ensure that all hard magnetic centers inside the dots are reversed. The sample was subsequently submitted either to a square inverse field $(-H)$ pulse generated by the electromagnet for long time (>10 s) measurements, or to a series of n successive similar negative pulses $(-H)$ with duration $\Delta t=24$ μs for shorter time measurements. The number of pulses n has been varied from 1 to 5×10^5, which means that the total field application time can be adjusted between 24 μs and 12 s.

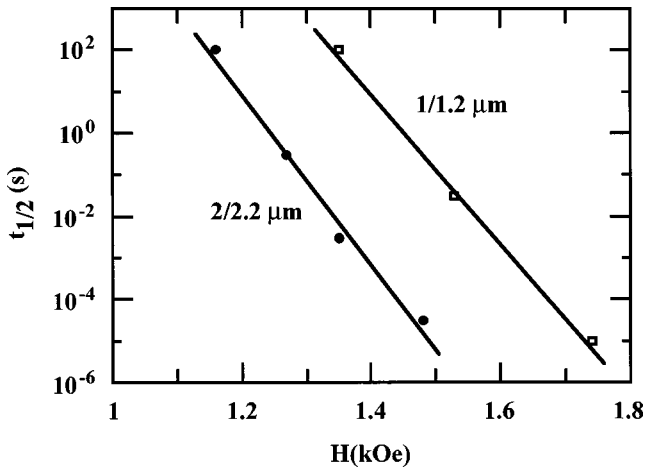

FIG. 11. Demagnetization time $t_{1/2}(H)$ as a function of H for the 1/1.2 μm and (b) 2/2.2 μm dot arrays. The solid lines are best fits to the experimental data.

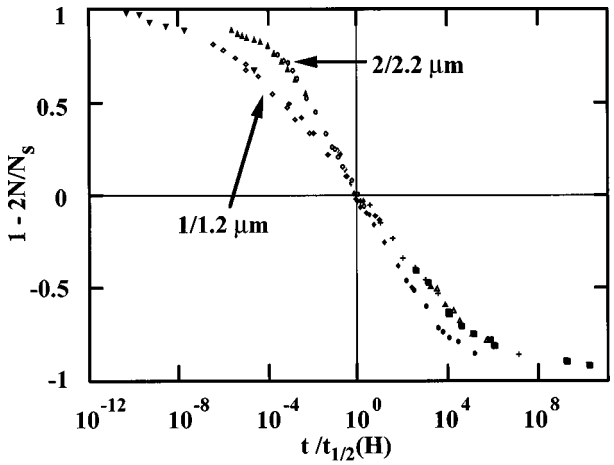

FIG. 12. Magnetic aftereffect in the 1/1.2 and 2/2.2 μm dot arrays as a function of the renormalized time $t/t_{1/2}(H)$. The data are extracted from Fig. 10.

We first carefully checked that the number of switched dots at a given field value, obtained either with the electromagnet or with the coil, was only dependent upon the total elapsed time t, within an accuracy of 10% compatible with all sources of possible errors.[30]

We then extracted the demagnetization time $t_{1/2}$ from the data of Fig. 10. The semilog plot presented in Fig. 11 demonstrates well that the exponential dependence of $t_{1/2}$ versus H, predicted by expression (9), is valid over a much larger field (or time) range than that considered above to deduce expressions (2). The variations of $t_{1/2}$ with H obtained from imaging data are

$$\begin{aligned} t_{1/2} &= 1.90\times 10^{26}\exp(-41.4H) \\ &\quad \text{for the 1/1.2 } \mu\text{m dot array,} \\ t_{1/2} &= 0.95\times 10^{26}\exp(-47.6H) \\ &\quad \text{for the 2/2.2 } \mu\text{m dot array.} \end{aligned} \tag{11}$$

Note that the parameters are slightly different from those of Eq. (2). This may be due to the fact that Eqs. (2) and (11) have been obtained by fitting over very different experimental time ranges, or this is related to experimental errors. Considering, for instance, our precision in field calibration, H is probably underestimated by 5% in imaging experiments with respect to PMOKE measurements.

Expression (11) also indirectly validate Eq. (4), i.e., our choice of a linear field dependence for the exponential argument in the mean switching time $\tau(H_n,H)$.

We can now define an activation length ξ_n, correlated to the activation volume V_n so that $V_n=\xi_n^2 t_{\mathrm{Co}}$, where t_{Co} is the average cobalt thickness. Following Eq. (9), we can estimate ξ_n from the coefficient of H in the exponential argument of expressions (11). We get, respectively, $\xi_n=25$ and 27 nm for the arrays with dots diameters of 1 and 2 μm. The two values are very close to each other, and are comparable to those obtained for Co/Au ultrathin films.[23] Note that ξ_n is far smaller than the dot size.

Finally, expression (10) predicts that for a given array the number of switched dots at different H values only depends upon the ratio $t/t_{1/2}(H)$. Indeed, all relaxation curves of Fig. 10 are found to fall on two universal plots (one for each array) over up to 20 decades of time (Fig. 12). This confirms again the previous hypothesis leading to expression (6).

Starting from expression (10), and as already demonstrated in Ref. 40, one finds that the derivative of the number of switched dots with respect to $\ln(t/t_{1/2}(H))$ is directly related to the nucleation field distribution function

$$\frac{dN(t,H)}{d\,\ln[t/t_{1/2}(H)]}=\frac{kT}{2M_sV_n}f\left(\overline{H}_n+\frac{kT}{2M_sV_n}\ln[t/t_{1/2}(H)]\right). \tag{12}$$

From the experimental data [Figs. 10(a) and 10(b)], one obtains for the 1/1.2 and 2/2.2 dot arrays almost symmetrical $f(H_n)$ distributions centered, respectively, around 1.967 and 1.640 kOe, with respective half widths at half maximum of 0.261 and 0.156 kOe (Fig. 13). In this figure, the amplitude of the distribution for the 1 μm dots has been multiplied by 4 to check the predictions of our model [see expression (13) below and the related discussion].

Let us now try to relate the respective nucleation field distributions $f_1(H_n)$ and $f_2(H_n)$ for the 1 and 2 μm dot arrays, to the nucleation field distribution $f_{\mathrm{CF}}(H_n)$ in the CF. At the beginning of Sec. IV, we put forward the argument that dot arrays can be envisioned as geometrical patterns superimposed on an ''initial continuous film'' with the same average properties as the CF area. Let us assume in this CF a random network of intrinsic nucleation sites, probably related to a distribution of structural defects in the film, and to which can be associated a distribution of nucleation fields $f_{\mathrm{CF}}(H_n)$ defined as above for the dot arrays. If the average distance between these nucleation sites is much smaller than a dot diameter, the patterned dot arrays can then be thought as sampling the intrinsic random distribution, with a precision depending on the dot diameter. We will call hereafter α_1 (respectively, α_2) the average number of nucleation sites inside a dot of diameter $d_1=1$ μm (respectively, $d_2=2$ μm). A reasonable assumption, considering the argument given

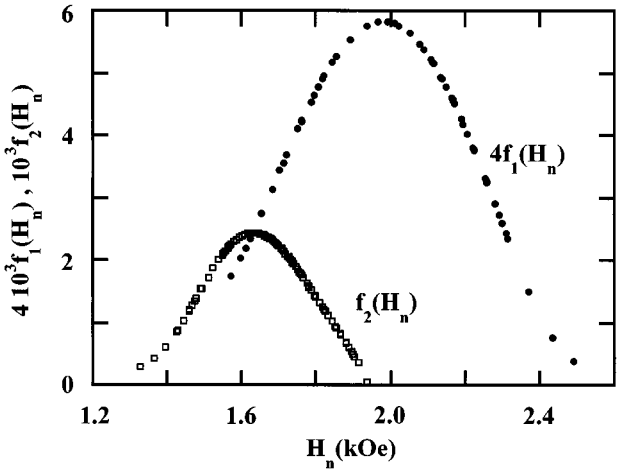

FIG. 13. Nucleation field distribution functions $f_1(H_n)$ and $f_2(H_n)$ of, respectively, the 1/1.2 and 2/2.2 μm dot arrays. For comparison with our theoretical predictions: $\alpha_2/\alpha_1=4$ (see text), we have plotted $4\times f_1(H_n)$. The data are extracted from a fit of the universal curves of Fig. 12.

above, is that those numbers are proportional to the area of the dots, which leads to the simple relation $\alpha_2=4\alpha_1$.

First, using a simple probability calculation (see the Appendix), the distribution function $f(H_n)$ of a dot array can be expressed as

$$f(H_n)=\alpha f_{\mathrm{CF}}(H_n)\left[\int_{H_n}^{\infty} f_{\mathrm{CF}}(H)dH\right]^{\alpha-1}, \tag{13}$$

where α can be either α_1 or α_2. Furthermore, the probability of finding coercive field of a given dot larger than H_n is given by

$$P(H_c \geqslant H_n)=\left[\int_{H_n}^{\infty} f_{\mathrm{CF}}(H)dH\right]^{\alpha}. \tag{14}$$

Note that both expressions (13) and (14) are strictly derived at $T=0$ K. From expression (14), we find that the probabilities to have the coercive field of a dot larger than H_n in the 1 and 2 micrometer dot arrays are related, so that

$$P_2(H_c \geqslant H_n)=[P_1(H_c \geqslant H_n)]^4. \tag{15}$$

From expression (13) one deduces that the ratio between the nucleation field distribution functions for the $d=2$ and 1 μm dots becomes

$$\frac{f_2(H_n)}{f_1(H_n)}=4\left[\int_{H_n}^{\infty} f_{\mathrm{CF}}(H)dH\right]^{3\alpha_1}. \tag{16}$$

Because the distribution function $f_{\mathrm{CF}}(H_n)$ is normalized to unity, this ratio is closely equal to 4 at low H_n values. As can be seen from Fig. 13, we find at low field H_n a reasonable agreement between the experimentally deduced distributions $f_2(H_n)$ and $4f_1(H_n)$. Therefore, we think that the low H_n part of the distribution functions displayed in Fig. 13 is closely proportional to the beginning of the f_{CF} distribution function, since for this part of the curves, we expect the integral raised to the power of $\alpha-1$ in expression (13) to be close to unity. Besides, it is clear from expression (13) that $f(H_n)$ tends towards $f_{\mathrm{CF}}(H_n)$ when α tends towards 1. This means that if we had only one possible nucleation center per dot, we would obtain the continuous film distribution. A way to get α closer to 1 would be to reduce the size of the dots.

Moreover, we now understand from expression (16) why the maximum of $f_1(H_n)$ for 1 μm dots occurs at a higher field than that of $f_2(H_n)$ for 2 μm dots. As a matter of fact, since the integral in Eq. (16) becomes smaller and smaller as the nucleation field H_n is increased, the ratio $f_2(H_n)/f_1(H_n)$ will rapidly decrease towards zero with increasing H_n.

C. Dynamic behavior—hysteresis loops

Having deduced the nucleation field distribution for each dot array, we are now able to rebuild the hysteresis loops displayed in Fig. 2. For that purpose, we just need the magnetic-field sweeping rate dH/dt (equal to 0.236 kOe/s in Fig. 2) as an extra parameter. Then, starting from a saturated state (for instance $M=-M_S$) at zero field (taken as the origin of time), and increasing the field so that $H(t)=(dH/dt)t$, the renormalized number of switched dots N/N_S at time t can be derived from expression (6). It is clear from this expression (6) that we need to know $f_1(H_n)$ and $f_2(H_n)$ for any positive values in order to calculate the integral. Unfortunately, as can be seen in Fig. 13, our experimental nucleation field distributions were obtained from the universal curves (Fig. 12) for which no information is available about the very beginning or the end of the reversal process (i.e., no experimental points are available close to $M/M_S=+$ or -1).

To overcome this problem, we used as a first approximation Gaussian fits for the $f_1(H_n)$ and $f_2(H_n)$ functions. The results are displayed in Fig. 14(a), and compared with experimental data: a very good agreement is obtained.

Note that, for the beginning and the end of the reversal, where the switching of only a few dots is involved, thermal fluctuations should become more important. As a result, if one kept on measuring hysteresis loops on the same area of the dot arrays and using the same experimental conditions, slight differences should be noticed at the beginning and at the end of the reversal. This will be clearly illustrated in a further paragraph and in Fig. 16.

Another way to calculate the hysteresis loops is to use expression (14) so that the normalized magnetization becomes $M(H)/M_S=1-2P(H \geqslant H_n)$ for $H>0$ [here H stands for H_c in expressions (14) and (15)]. There, we need to assume an analytical shape for f_{CF}, and to chose α_1 and α_2. It must be stressed that this is a tricky problem since we have an unknown quantity which is a number and another one which is a function. It then has an *a priori* infinite set of solutions (f_{CF},α). Thus we cannot reasonably find the proper f_{CF} distribution from the hysteresis loop measurements. It is nevertheless possible to check the expression linking α_2 to α_1, or equivalently the expression (15), and to obtain a reasonable order of magnitude for α_1 and α_2. For this purpose we tried two different possible shapes for $f_{\mathrm{CF}}(H_n)$, which both display an initial rise compatible with $f_1(H_n)$ and $f_2(H_n)$. The first shape used two semi-Gaussian functions centered on H_0 and with left and right standard

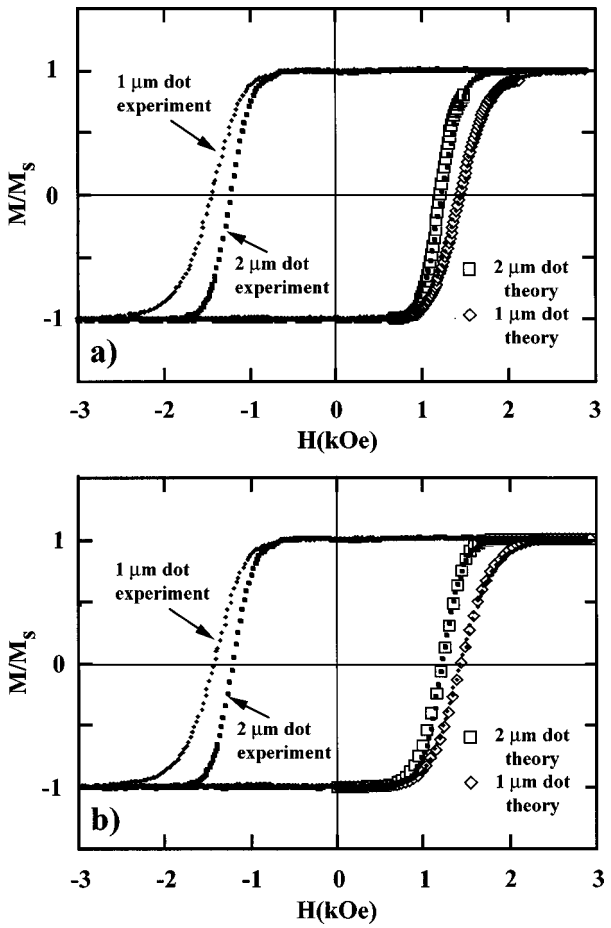

FIG. 14. Comparison between the experimental hysteresis loops for the 1/1.2 and 2/2.2 μm dot arrays (Fig. 2) and their calculation assuming a Gaussian distribution of nucleation fields (a) or a pseudo-Gaussian assymetric distribution (b). In this last case a very good fit is obtained for parameters reported in the text.

deviations ΔH_1 and ΔH_2. The second shape was a cosine-type function $f_{CF}(H_n)=g[1-\cos(\theta)]^2$ with $g=2/[3(H_{max}-H_{min})]$ and $\theta=2\pi(H_n-H_{min})/(H_{max}-H_{min})$, bounded to the interval $[H_{min},H_{max}]$ and being zero elsewhere. Three adjustable parameters are needed for the semi-Gaussian distribution function, and two for the cosine one. The same procedure was used in both cases to find the appropriate α_1 and α_2 values: we start from the highest possible value of α_1, i.e., $\alpha_1=(\pi/4)(d_1/\xi_n)^2$ for the $d_1=1$ μm dots, and determine the parameters of the f_{CF} functions which give the best fit of the hysteresis loops displayed in Fig. 2.; α_1 is then reduced and the new sets of parameters are found. At the end, one keeps the couple (f_{CF},α_1) which gives the best fit. α_2 is then obtained by trying to get the best fit of the 2 μm dots hysteresis loops, using the same ''best'' f_{CF} function. Let us remark that to assume $\alpha_1=(\pi/4)$ $(d_1/\xi_n)^2$ is equivalent to the statement that the average distance between nucleation centers, defined by $\ell_1=(\pi d_1^2/4\alpha_1)^{1/2}$, is equal to ξ_n.

The first point worthy of notice is that, for both functions, the approach to saturation in the 1 μm dot array hysteresis loop can only be well fitted for an α_1 value smaller than 50. The best fit is found for α_1 close to 5, and is nearly independent of the chosen distribution function f_{CF}. The average number of nucleation centers inside a 1 μm dot is thus of the order of 5 in our experimental conditions, and the average distance between nucleation centers is estimated to be $\ell_1=(\pi d_1^2/4\alpha_1)^{1/2}=396$ nm.

The second interesting point is that, to deduce the proper coercive field for the 2 μm dots, it is always necessary to take $\alpha_2=3\alpha_1$, instead of $\alpha_2=4\alpha_1$ as expected from our simple theory. Then, for the 2 μm dots we obtain $\alpha_2=15$, corresponding to an average distance between nucleation centers $\ell_2=458$ nm, for H close to the corresponding coercive field of 1.2 kOe. Fits are displayed in Fig. 14(b) in the case of a semi-Gaussian shape with $\alpha_1=5$ and $\alpha_2=15$ and H_0, ΔH_1, and ΔH_2 taken equal to 1.7, 0.35, and 0.95 kOe, respectively. The reason why $\alpha_2/\alpha_1=3$ can be a reduction of the nucleation field value at the edge of the dots, due to the etching process.

As a conclusion to this section, it is important to note that we have been able to deduce two characteristic lengths for the nucleation process in our system, ξ_n representing the typical size of a nucleation center and ℓ giving the typical distance between nucleation centers. As far as ℓ is concerned, it is the typical length between nucleation centers in the ''initial continuous film,'' provided that the patterning process preserves the homogeneity of the spatial distribution of the nucleation centers inside all dots.

D. Thermal fluctuations of the nucleation probability

As we mentioned above, the magnetization of the dots arrays, as well as the number of magnetically switched dots, are not exactly reproducible after similar experimental procedures. This comes from statistical fluctuations in the magnetization reversal of a dot, and is well illustrated in Fig. 15 over a restricted array area of 100 dots. The figure displays the switched dots configuration after nine successive tests performed under the same (H,t) experimental conditions. If up to 56 dots have been switched at least one time, thermal fluctuations control the reversal of a rather large number of 13 dots labeled a–m. However, even though we observe a very limited area, the integrated magnetization varies only within $\pm 5\%$ of the average value. For a given dot of the array exhibiting a square hysteresis loop, the switching (or nucleation) field probability P_{SW} is plotted as a function of H in Fig. 16. Assuming that the nucleation field is larger than the propagation field in the first stage of the reversal, and that the nucleation area is not larger than that of an elementary cell, one can say that we are mainly probing the magnetization reversal of a 25 nm$\times$25 nm$\times$1 nm single-domain particle.

V. CONCLUSION

We have reported a comprehensive experimental and theoretical study of magnetization reversal in Au/Co(1 nm)/Au dot arrays. In continuous Au/Co(1 nm)/Au films, magnetization reversal is dominated by easy domain-wall propagation, following the first few nucleation events. We have shown here that patterning arrays of Au-Co-Au dots with decreasing diameter amounts to sampling with increasing precision the distribution of nucleation sites in the initial film, as domain-wall propagation is blocked at the edge of the dot. On this basis, we have developed a detailed statistical model that

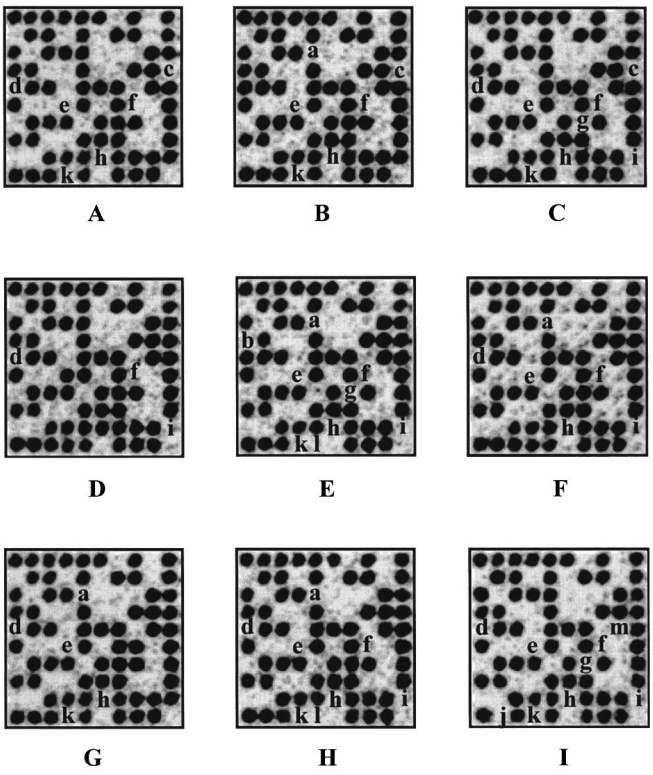

FIG. 15. Magneto-optical imaging of the same set of 100 dots in the 2/2.2 μm dot array under the same experimental conditions. After saturation ($H_s=+2.5$ kOe) giving black dots, the same reversed field ($H=-1.35$ kOe) has been applied to the sample during the same time ($\Delta t=0.73$ ms). On these images, switched dots cannot be distinguished from the gray background. This experiment has been repeated nine times (images A to I). The letters indicate dots which do not always switch.

allowed us to extract from the experimental data a picture of the nucleation field distribution, and evaluate two fundamental lengths: the nucleation length ξ_n (which scales the lateral dimension of a nucleation volume), and the mean distance ℓ between nucleation sites. We finally showed that our method allows one to track nanometer scale magnetic events (a nucleation event) using micrometer-scale resolution experiments (far-field MO imaging). The easy-wall propagation that reverses the entire dot after a single nucleation acts here as an amplifying detector.

Although developed here for a specific case, both our experimental approach and theoretical treatment can be extended to other systems and configurations. More generally, we consider our work as an example of how microfabrication can help to understand magnetization reversal in continuous films.

APPENDIX

We have to calculate the probability $f(H_n)dH_n$ that a dot of diameter d has a nucleation field included in the interval $[H_n, H_n+dH_n]$. We note α the average number of nucleation centers per dot. Each of these centers is characterized by a nucleation field H_n with probability $f_{\mathrm{CF}}(H_n)dH_n$, where $f_{\mathrm{CF}}(H_n)$ is the nucleation field distribution for the continuous film. Besides, since in the full dot array there is a

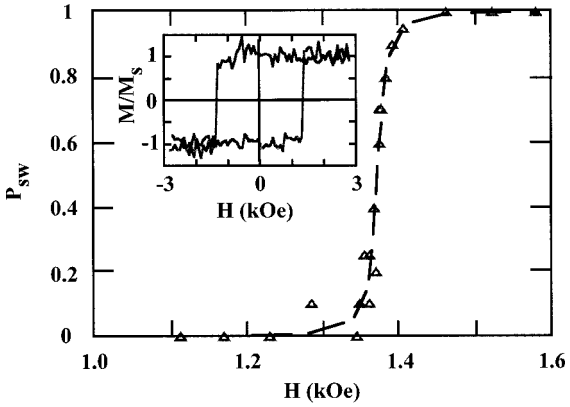

FIG. 16. Magnetization-reversal probability P_{SW} for one of the dots of the 1/2 μm dot array. The insert displays the hysteresis loop of this particular dot.

finite (but very high) number P of possible nucleation fields we will index them so that $H_{n1}<H_{n2}<\cdots<H_{nP}$.

In the following $T=0$ K calculation, one assumes that, in a dot having an experimental switching field H_{nj}, at least one of the α centers is characterized by a nucleation field H_{nj}, while no other center has a nucleation field H_{nk} so that $k<j$.

To simplify calculations we will first consider the simple case $\alpha=3$, $P=5$. In that case, one states that there exists only five possible nucleation fields for the full dot array, $H_{n1}<H_{n2}<H_{n3}<H_{n4}<H_{n5}$, and each dot contains, on average, three possible nucleation centers. For instance, we will look for the probability that a given dot nucleates at a field H_{n3}. Then, it is necessary to look at the probability of appearance of all possible configurations.

If only one of the $\alpha=3$ nucleation centers has a nucleation field H_{n3}, then according to the above $T=0$ K hypothesis, the two other centers have necessarily nucleation fields equal to H_{n4} or H_{n5}. The probability for obtaining this configuration is given by $3[f_{\mathrm{CF}}(H_{n3})f^2_{\mathrm{CF}}(H_{n4})+f_{\mathrm{CF}}(H_{n3})f^2_{\mathrm{CF}}(H_{n5})+f_{\mathrm{CF}}(H_{n3})f_{\mathrm{CF}}(H_{n4})f_{\mathrm{CF}}(H_{n5})]$. Note that, since we consider so far a discrete model for H_n, the probability $f_{\mathrm{CF}}(H_n)dH_n$ has been replaced by $f_{\mathrm{CF}}(H_n)$. In the same way, the situation for which two among the $\alpha=3$ nucleation centers have the nucleation field H_{n3} has the probability $3[f^2_{\mathrm{CF}}(H_{n3})f_{\mathrm{CF}}(H_{n4})+f^2_{\mathrm{CF}}(H_{n3})f_{\mathrm{CF}}(H_{n5})]$, and finally, the $\alpha=3$ nucleation centers can all have the nucleation field H_{n3} with probability $f^3_{\mathrm{CF}}(H_{n3})$. Then, the total probability that a given dot has a nucleation field H_{n3} is simply the sum of the three above probabilities. It can easily be seen that this sum may be rewritten as

$$\left[\sum_{h=3}^{5} f_{\mathrm{CF}}(H_{nh})\right]^3-\left[\sum_{h=4}^{5} f_{\mathrm{CF}}(H_{nh})\right]^3. \tag{A1}$$

It is straightforwards to generalize this expression (A1) for any values of P and α. We obtain

$$\left[\sum_{h\geqslant j} f_{\mathrm{CF}}(H_{nh})\right]^{\alpha}-\left[\sum_{h>j} f_{\mathrm{CF}}(H_{nh})\right]^{\alpha}, \tag{A2}$$

which becomes, in the continuous limit

$$f(H_n)dH_n=\left(\int_{H_n}^{\infty} f_{\mathrm{CF}}(H)dH\right)^{\alpha}-\left(\int_{H_n+dH_n}^{\infty} f_{\mathrm{CF}}(H)dH\right)^{\alpha}. \tag{A3}$$

We can notice that the right member of expression (A3) expresses the inverse of the slope of the function

$$F(H_n)=\left(\int_{H_n}^{\infty} f_{\mathrm{CF}}(H)dH\right)^{\alpha}. \tag{A4}$$

Expression (A3) then becomes

$$f(H_n)=\alpha f_{\mathrm{CF}}(H_n)\left[\int_{H_n}^{\infty} f_{\mathrm{CF}}(H)dH\right]^{\alpha-1}. \tag{A5}$$

To find the probability $P(H_c \geqslant H_n)$ that the nucleation field of a given dot is larger than a given H_n, we simply notice that $d[P(H_c \geqslant H_n)]/dH_n=-f(H_n)$.

[1] M. A. M. Gijs, S. K. J. Lenczowski, B. Gierbers, R. J. M. Van de Veerdonk, M. T. Johnson, R. M. Jungblut, A. Reinders, and R. M. J. Van Gansewinkel, J. Magn. Magn. Mater. **151**, 333 (1995).

[2] T. L. Hylton, M. A. Parker, K. R. Coffey, J. K. Howard, R. Fontana, and C. Tsang, Appl. Phys. Lett. **67**, 1154 (1995).

[3] P. R. Krauss, P. B. Fischer, and S. Chou, J. Vac. Sci. Technol. B **12**, 3639 (1994).

[4] R. M. H. New, R. F. W. Pease, and R. L. White, J. Vac. Sci. Technol. B **12**, 3196 (1994).

[5] S. Chou, Data Storage **1995**, 35 (1995).

[6] A. Fernandez, P. J. Bedrossian, S. L. Barker, S. P. Vernon, and D. R. Kania, IEEE Trans. Magn. **32**, 4472 (1996).

[7] L. Kong, L. Zhuang, and S. Chu, IEEE Trans. Magn. **33**, 3019 (1997).

[8] M. Hehn, K. Ounadjela, S. Padovani, J. P. Bucher, J. Arabski, N. Bardou, B. Bartenlian, C. Chappert, F. Rousseaux, D. Decanini, F. Carcenac, E. Cambril, and M. F. Ravet, J. Appl. Phys. **79**, 5068 (1996); M. Hehn, K. Ounadjela, J. P. Bucher, F. Rousseaux, D. Decanini, B. Bartenlian, and C. Chappert, Science **272**, 1782 (1996).

[9] C. Miramond, C. Fermon, F. Rousseaux, D. Decanini, and F. Carcenac, J. Magn. Magn. Mater. **165**, 500 (1997).

[10] G. A. Gibson and S. Schultz, J. Appl. Phys. **73**, 4516 (1993).

[11] A. Maeda, M. Kume, T. Ogura, K. Kuroki, T. Yamada, M. Nishikawa, and Y. Harada, J. Appl. Phys. **76**, 6667 (1994).

[12] O. Geoffroy, D. Givord, Y. Otani, B. Pannetier, and F. Ossart, J. Magn. Magn. Mater. **121**, 223 (1993).

[13] F. Rousseaux, D. Decanini, F. Carcenac, E. Cambril, M. F. Ravet, C. Chappert, N. Bardou, B. Bartenlian, and P. Veillet, J. Vac. Sci. Technol. B **13**, 2787 (1995).

[14] R. M. H. New, R. F. W. Peare, and R. L. White, J. Vac. Sci. Technol. B **13**, 1089 (1995).

[15] S. Gadetsky, T. Suzuki, J. K. Erwin, and M. Mansuripur, IEEE Trans. Magn. **30**, 4404 (1994); S. Gadetsky, J. K. Erwin, M. Mansuripur, and T. Suzuki, J. Appl. Phys. **79**, 5687 (1996).

[16] S. Gider, J. Shi, D. D. Awschalon, P. F. Hopkins, K. L. Campman, A. C. Gossard, A. D. Kent, and S. von Molnar, Appl. Phys. Lett. **69**, 3269 (1996).

[17] D. D. Awschalom, D. P. Di Vicenzo, and J. F. Smyth, Science **258**, 414 (1992).

[18] R. Gupta, J. J. Mac Clelland, Z. J. Jabbour, and R. J. Celotta, Appl. Phys. Lett. **67**, 1378 (1995).

[19] M. Pardavi-Horvath, IEEE Trans. Magn. **32**, 4458 (1996).

[20] N. Bardou, B. Bartenlian, C. Chappert, R. Mégy, P. Veillet, J. P. Renard, F. Rousseaux, M. F. Ravet, J. P. Jamet, and P. Meyer, J. Appl. Phys. **79**, 5848 (1996).

[21] V. Grolier, J. Ferré, A. Maziewski, E. Stefanowicz, and D. Renard, J. Appl. Phys. **73**, 5939 (1993).

[22] J. Pommier, P. Meyer, G. Penissard, J. Ferré, P. Bruno, and D. Renard, Phys. Rev. Lett. **65**, 2054 (1990).

[23] A. Kirilyuk, J. Ferré, and D. Renard, Europhys. Lett. **24**, 403 (1993).

[24] C. Cesari, J. Faure, G. Nihoul, K. Le Dang, P. Veillet, and D. Renard, J. Magn. Magn. Mater. **78**, 296 (1989).

[25] Y. Chen, R. K. Kupka, F. Rousseaux, F. Carcenac, D. Decanini, M. F. Ravet, and H. Launois, J. Vac. Sci. Technol. B **12**, 3959 (1994).

[26] N. Bardou, B. Bartenlian, F. Rousseaux, D. Decanini, F. Carcenac, E. Cambril, M. F. Ravet, C. Chappert, P. Veillet, P. Beauvillain, R. Megy, W. Geerts, and J. Ferré, J. Magn. Magn. Mater. **156**, 139 (1996).

[27] J. Badoz, M. Billardon, J. C. Canit, and M. F. Russel, J. Opt. (Paris) **8**, 373 (1977).

[28] K. Sato, Jpn. J. Appl. Phys. **20**, 2403 (1981).

[29] N. Bardou, B. Bartenlian, F. Rousseaux, D. Decanini, F. Carcenac, C. Chappert, P. Veillet, P. Beauvillain, R. Megy, Y. Suzuki, and J. Ferré, J. Magn. Magn. Mater. **148**, 293 (1995).

[30] A. Kirilyuk, J. Ferré, V. Grolier, J. P. Jamet, and D. Renard, J. Magn. Magn. Mater. **171**, 45 (1997).

[31] J. Ferré, V. Grolier, P. Meyer, S. Lemerle, A. Maziewski, E. Stefanowicz, S. V. Tarasenko, V. V. Tarasenko, M. Kisielewski, and D. Renard, Phys. Rev. B **55**, 15 092 (1997).

[32] J. Ferré, J. P. Jamet, J. Pommier, P. Beauvillain, C. Chappert, R. Mégy, and P. Veillet, J. Magn. Magn. Mater. **174**, 77 (1997).

[33] M. Labrune, S. Andrieu, F. Rio, and P. Bernstein, J. Magn. Magn. Mater. **80**, 211 (1989).

[34] N. Bardou, Ph.D. thesis, Université Paris-Sud, Orsay, France, 1996.

[35] L. Néel, Ann. Geophys. (C.N.R.S.) **5**, 99 (1949).

[36] M. Lederman, S. Schultz, and M. Ozaki, Phys. Rev. Lett. **73**, 1986 (1994).

[37] W. Wernsdorfer, K. Hasselbach, A. Sulpice, A. Benoit, J. E. Wegrowe, L. Thomas, B. Barbara, and D. Mailly, Phys. Rev. B **53**, 3341 (1996).

[38] W. F. Brown, Jr., Phys. Rev. **130**, 1677 (1963).

[39] W. Wernsdorfer, E. Bonet Orozco, K. Hasselbach, A. Benoit, B. Barbara, N. Demoncy, A. Loiseau, H. Pascard, and D. Mailly, Phys. Rev. Lett. **78**, 1791 (1997).

[40] K. O'Grady, M. El-Hilo, and R. W. Chantrell, J. Appl. Phys. **76**, 6368 (1994).